Fabrication and dc characteristics of small-area tantalum and niobium superconducting tunnel junctions

D. W. Face[a] and D. E. Prober
Section of Applied Physics, Yale University, P. O. Box 2157, New Haven, Connecticut 06520

(Received 16 March 1987; accepted for publication 18 June 1987)

We discuss the fabrication and dc electrical characteristics of small-area (1–$6\,\mu m^2$) superconducting tunnel junctions with Ta or Nb base electrodes and Pb or $Pb_{0.9}Bi_{0.1}$ counterelectrodes. These junctions have very small subgap leakage currents, a "sharp" current rise at the sum-gap voltage, and show strong quantum effects when used as microwave mixers. The use of a low-energy (~ 150 eV) ion cleaning process and a novel step-defined fabrication process that eliminates photoresist processing after base electrode deposition are discussed. Tunnel barriers formed by dc glow discharge oxidation were the most successful. Tunnel barrier formation by thermal oxidation and ion-beam oxidation is also discussed. An oxidized Ta overlayer (~ 7 nm thick) was found to improve the characteristics of Nb-based junctions. The electrical characteristics of junctions with different electrode and barrier materials are presented and discussed in terms of the physical mechanisms that lead to excess subgap current and to a width of the current rise at the sum-gap voltage.

I. INTRODUCTION

Superconductor-insulator-superconductor (SIS) quasiparticle mixers provide nearly quantum-limited sensitivity for the detection of millimeter wavelength radiation.[1–4] Schottky barrier mixers, the closest competing technology, have significantly more noise and require more local oscillator power than SIS mixers. SIS mixers are presently used in many practical radioastronomical receivers[4–6] and have been well reviewed.[1]

Essential to the study of strong quantum effects in SIS mixers is the controlled fabrication of small-area ($\sim 1\,\mu m^2$), high-current density ($\sim 1000\,A/cm^2$) tunnel junctions with nearly ideal current versus voltage (I-V) characteristics. The small area is required to keep the junction capacitance small, $C_J \sim 300$ fF, while the high current density is required to simultaneously produce a junction resistance of 50–100 Ω for efficient coupling at the signal and intermediate frequencies. The nearly ideal I-V characteristics are required to produce a mixer with low noise, approaching the quantum limit, and a large conversion efficiency. In addition, a practical tunnel junction must be stable and must withstand repeated thermal cycling from room temperature to liquid-helium (LHe) temperatures.

Junction technologies based on refractory metal electrodes, typically niobium, are currently the most successful in meeting the practical requirements of stability and temperature cyclability,[7] but have not been widely used in mixer applications. Junctions with Nb base electrodes and soft (e.g., Pb) counterelectrodes generally use Nb-oxide tunnel barriers. On the other hand, Nb based junctions with Nb counterelectrodes generally employ artificial barriers (e.g., amorphous Si, or Al/Al oxide).[7] An alternative approach which uses a PbBi base electrode and an In-oxide barrier has also been developed[8] and shows promise for some mixer applications. Despite the practical advantages of junctions using refractory films, to date the well-established Pb-alloy process developed by IBM[9] is most commonly used to fabricate tunnel junctions for mixer applications.[4,5] Acceptable electrical characteristics are obtained with these all Pb-alloy junctions, although strong quantum effects are not generally observed.

In a recent publication,[3] we reported briefly on a new junction technology that employs a refractory base electrode, Ta, and a $Pb_{0.9}Bi_{0.1}$ counterelectrode, for the fabrication of SIS mixers. These junctions have nearly ideal BCS I-V characteristics, survive repeated thermal cycling, and display strong quantum effects when used as mixers at 36 GHz. A receiver noise temperature of 24 K obtained with these junctions[3] is the lowest reported at this frequency. In essence, the Ta base electrode and oxide have the same robustness as achieved with Nb, but the Ta oxide is a much higher-quality tunnel barrier than Nb oxide. The lower T_c of Ta, ~ 4.3 K, is acceptable for mixer applications where pumped LHe is used to achieve $T \leqslant 2$ K.

Microwave mixing results obtained with the Ta based junctions[10,11] demonstrate the importance of I-V "sharpness" and small subgap leakage currents for observing strong quantum effects. Figure 1 shows a schematic I-V curve, where we define the junction parameters which characterize the "sharpness" and leakage current. The "sharpness" of the junction is characterized by the voltage width ΔV of the current rise at the sum-gap voltage V_G. For mixer applications, an I-V curve is considered to be "sharp" when ΔV is less than $\hbar\omega/e$ for the frequency of interest ($\hbar\omega/e \simeq 150\,\mu V$ at 36 GHz). The subgap leakage current, I_{sg} is measured at 80% of V_G and must be small compared to ΔI for the mixer noise to approach the quantum limit.

In this paper, we present a detailed description of the fabrication process for Ta- and Nb-based junctions. A number of special fabrication techniques, such as the use of a thin (< 20 nm thick) Nb underlayer for the nucleation of Ta base electrode films in the bcc (superconducting) phase are discussed. The dc electrical characteristics of a number of $Ta/Pb_{0.9}Bi_{0.1}$, Ta/Pb, and $Nb/Pb_{0.9}Bi_{0.1}$ tunnel junctions are presented. References 10 and 11 discuss a quantitative

[a] Present address: Dept. of Physics, MIT, Rm. 13-2145, Cambridge, MA 02139.

 0021-8979/87/203257-10$02.40 © 1987 American Institute of Physics

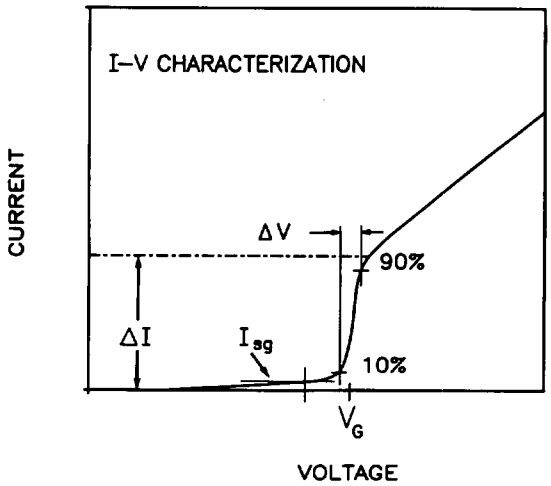

FIG. 1. Model I-V curve showing the definitions of ΔV, I_{sg}, and ΔI used in Table II. The gap voltage $V_G = (\Delta_1 + \Delta_2)/e$.

comparison of results for mixer experiments using junctions with "sharp" and "rounded" I-V curves.

II. JUNCTION FABRICATION

The fabrication process used for all of the Ta and Nb junctions in this paper employs a step-defined process which is illustrated in Figs. 2 and 3. The use of this technique eliminates photoresist processing between critical junction formation steps. The process described below is optimized for Ta junctions, and is summarized in Table I. Variations of this process for Nb based junctions and for different barrier formation techniques are presented later, in the section on dc I-V curves. Typical junction areas are $\sim 2\,\mu m^2$.

A. Photolithography and reactive ion etching

The fabrication process begins by patterning a series of Cr lines which are 1–2 μm wide and $\sim$50 nm thick, using contact photolithography on a standard 2-in.-diam Si (100) wafer. The lines are placed end to end on 914 μm (36 mil) centers, as illustrated in a top view in Fig. 2(a). The Cr serves as an etch mask during subsequent reactive ion etching (RIE) which is used to define a 0.7-μm-high step in the Si substrate [see Fig. 3(a)].

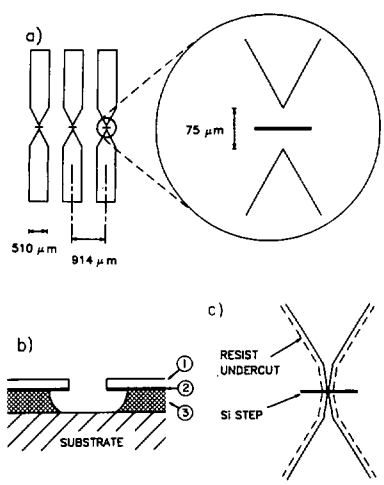

FIG. 2. (a) Top view of the electrode lead pattern (in the top layer of photoresist) approaching to within 75 μm of the reactive ion etch (RIE) defined step in the Si substrate. (b) Cross section of the trilayer resist structure after developing the top layer (1), etching the Al isolation layer (2), and developing the bottom layer (3). (c) Top view of the trilayer resist structure after all patterning is complete. The structure is now ready for metal deposition as shown in Figs. 3(b)-3(d).

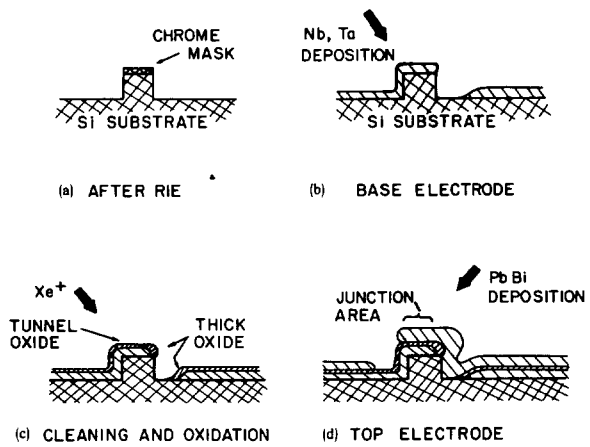

FIG. 3. (a) Si substrate after reactive ion etching (RIE). (b) Base electrode sputter deposition after trilayer photoresist patterning shown in Fig. 2. (c) Low-energy ($\sim$150 eV) Xe ion cleaning and glow discharge oxidation. Note the thick oxide used for edge protection. (d) Counterelectrode deposition to complete the junction. See Fig. 4 for a perspective drawing of the completed junction after liftoff.

The 13.56-MHz rf power for RIE is capacitively coupled with a tuneable rf matching network. Unlike most RIE processes, we apply a small amount of rf power to the upper electrode. This gives the upper electrode a self-bias of ~ -100 V while the lower electrode operates with a self bias of ~ -300 V. The purpose of the small self bias on the upper electrode is to continuously etch the upper surface clean to prevent polymer buildup. Applying power to the upper electrode gave a remarkable improvement in the smoothness of the Si wafer after etching, as compared to results with an unpowered upper electrode. With these considerations in mind, our standard Si etching process uses the following conditions: chamber pressure $\simeq$0.47 Pa, rf power $\simeq$30 W, CF_3Br flowrate$\simeq$8 sccm, O_2 flow rate$\simeq$0.9 sccm. Under these conditions, we find a Si etch rate of $\sim$50 nm/min. After RIE, the Cr film is removed with a wet chemical etch.

A trilayer photoresist structure is used to pattern the superconducting films. The trilayer resist consists of an exposed 1.5-μm-thick bottom layer of Shipley MP1350J, a 50-

TABLE I. Summary of processing steps for the step-defined junction fabrication process.

1. Pattern Cr line, etch the step in the Si substrate with reactive ion etching (RIE), and remove Cr with wet etch.
2. Prepare the trilayer resist structure.
3. Expose and develop the top layer of the trilayer resist, etch the Al isolation layer, and develop the bottom layer for an undercut resist profile [Figs. 2(b) and 2(c)].
4. Deposit the base electrode (Ta or Nb) by ion-beam sputtering [Fig. 3(b)].
5. Form a thick oxide by air exposure for $\sim$ 2 h.
6. Low-energy ion cleaning and dc glow discharge oxidation [Fig. 3(c)].
7. Evaporate the $Pb_{0.9}Bi_{0.1}$ counterelectrode [Fig. 3(d)].
8. Liftoff the metal films to complete the patterning (Fig. 4).

nm-thick Al isolation layer, and a 1.0-μm-thick top layer of MP1370 photoresist [see Fig. 2(b)]. In this resist structure, the top layer is intended for pattern exposure. The bottom layer provides an undercut resist profile after exposure and development, as shown in Fig. 2(b). The undercut profile of Fig. 2(b) allows relatively thick ($\sim$500 nm) metal films to be deposited. The metal film on top of the resist is then easily removed (lifted off) by dissolving the resist stencil in acetone. This liftoff process leaves a patterned metal film on all regions of the substrate where the resist stencil was previously exposed and developed.

To expose the trilayer resist, a contact mask is first used to define the lead geometry which narrows to a gap within $\sim$37 μm of the steps, as shown in Fig. 2(a). After developing this pattern in the top layer only, the high-resolution portion of the final pattern is exposed in the top layer by projection lithography,[12] and then developed. The Al isolation layer is then etched and the bottom layer developed to produce a controlled undercut, as indicated by the final pattern in Figs. 2(b) and 2(c). This three layer stencil now defines a 1–2-μm-wide slot over the Si step where the tunnel junction will be formed. On each side of the step, the slot flares out to 510-μm-wide strips which will form the leads to the junction.

B. Film deposition and tunnel barrier formation

The 300-nm-thick Ta (or Nb) base electrode is deposited by ion-beam sputtering[13] at a 45° angle. This leaves a break in the shadow of the step as shown in Figs. 3(b) and 4.

It is generally not easy to produce Ta films in the bcc (superconducting) crystal structure on room-temperature substrates. In fact, Ta films that are ion-beam deposited directly onto Si substrates always grow in the β-Ta phase (tetragonal crystal structure). The β-Ta phase is undesirable because it is not superconducting above 1 K and has a high resistivity, $\sim$150 $\mu\Omega$ cm. The methods we developed for nucleating bcc Ta are discussed in detail in Ref. 13. In brief, we always deposit a thin Nb underlayer immediately before the Ta film deposition, in order to nucleate the Ta film in the bcc (superconducting) phase without the use of substrate heating.[13] In our experience, Nb films always grow in the bcc crystal structure. The lattice constant of bulk Nb is only 0.1% smaller than that of bulk bcc Ta. The close lattice match between Nb and Ta may favor the growth of Ta in the bcc structure on a thin Nb underlayer. A more detailed account of the properties of our bcc and β-Ta films is presented separately.[13]

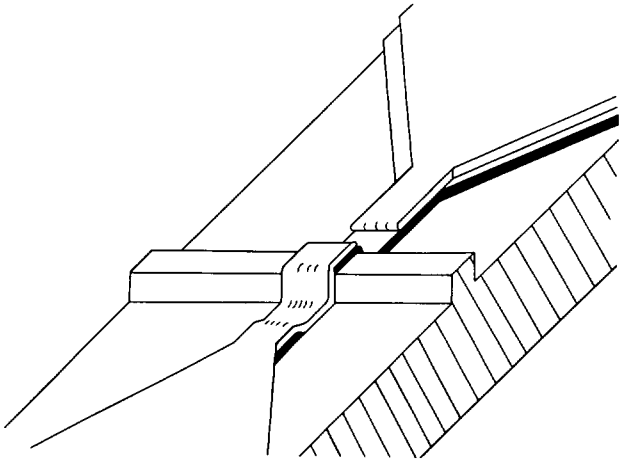

FIG. 4. Perspective drawing of the step edge junction after completion. The tunnel junction is on top of the step.

Following the Ta deposition, a thick oxide layer is grown over the entire Ta film by intentional exposure to air for 1–2 h. The sample is then loaded into a *separate* vacuum system for junction cleaning, oxidation, and counterelectrode deposition. This separate vacuum system is pumped to a pressure of $< 1 \times 10^{-4}$ Pa. Although the process sequence we have developed could, in theory, be carried out in a single vacuum chamber, we found it prudent to avoid the evaporation of Pb in the ion-beam deposition system. Thus, cross contamination is avoided.

The second vacuum system is equipped with a small Kaufman ion source, which is used to clean the surface of the Ta film with low-energy (160 eV) Xe^+ ions at a current density of $\sim$100 μA/cm^2 for 3 min. Low voltage sputter yields of Ta and Ta_2O_5 (Ref. 14) give a calculated Xe gas sputter rate of $\sim$2.5 nm/min for Ta_2O_5 and 1.2 nm/min for Ta at 160 eV, both for an ion current density of 130 μA/cm^2. Based on these calculated values, a cleaning time of $\sim$3 min was judged to be sufficient. Junctions made by cleaning and not oxidizing always produced shorts when a 3-min cleaning time of the Ta surface was employed. This indicates that the surface was sufficiently clean after a 3-min ion cleaning.

The Xe^+ ion-beam impinges on the surface from the same angle that the Ta film was originally deposited. As illustrated in Fig. 3(c), this process leaves a thick oxide layer on the shadowed edge of the film at the break and thus eliminates tunneling into this region. The region at the Ta/Nb/Si interface on the edge of the film with the thick oxide layer may have a reduced energy gap voltage due to damage and/or intermixing. If not covered by the thick oxide, this region would contribute to an increased voltage width ΔV of the current rise at the sum gap, due to the locally reduced gap voltage. This increased ΔV would thus degrade the mixer performance. All photoresist layers which are exposed to the ion beam during cleaning are covered with a Ta film. This helps to reduce contamination of the junction surface due to photoresist sputtering during cleaning.

After cleaning, the Ta surface is reoxidized in an oxygen dc glow discharge for 10–30 s, depending on the current density J_c desired. The glow discharge uses a pressure of 17 Pa of flowing O_2, with a voltage of $-$ 390 V applied to an Al plate below the sample. The discharge current is $\sim$3 mA. A plot of the junction critical current density J_c versus oxidation time is given in Fig. 5 for numerous samples. The reproducibility is better than a factor of 2. This is quite adequate for the present studies. Junctions made with the glow discharge oxidation technique have nearly ideal I-V characteristics, even at a current density of 1300 A/cm^2. In addition, the lack of a proximity effect "knee"[15] at the sum gap indicates a well-defined interface between each electrode and the tunnel barrier.

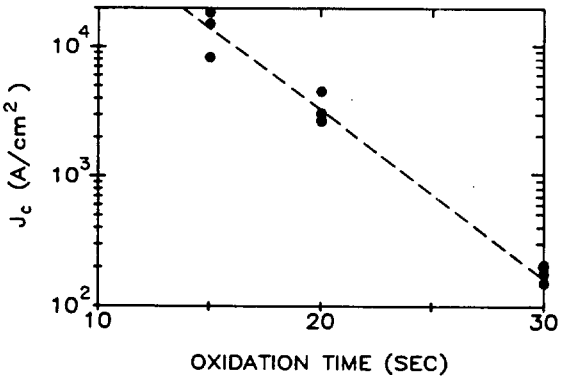

FIG. 5. Plot of critical current density vs oxidation time for Ta junctions produced with the glow-discharge oxidation process.

The success of the glow-discharge process can be understood by recognizing that the ion energies at the junction surface are on the order of the plasma potential (<20 eV), which is low for plasma processes.[16] In addition, the higher pressure (compared to ion-beam oxidation discussed below) allows the process to be less directional and more isotropic due to the shorter mean free path, which is $\sim 400\,\mu$m at 17 Pa. This nondirectionality also eliminates the edge shadowing effects which may have caused the reproducibility problems with ion-beam oxidation (see below). Without the glow discharge, the thermal oxidation rate with O_2 at a pressure of 17 Pa is found to be negligible. In fact, attempts to thermally oxidize the Ta surface (after ion-beam cleaning) with pressures up to 17 kPa of O_2 always produced low-resistance, $<10\,\Omega$, junctions.

Following oxidation, the substrate is rotated and a 300-nm $Pb_{0.9}Bi_{0.1}$ counterelectrode is evaporated from an alloy source at ~ 5 nm/s, as shown in Fig. 3(d). Alloy compositions in this paper are given in weight percent. The $Pb_{0.9}Bi_{0.1}$ (fcc phase) alloy composition was chosen because it exists as single phase material over a reasonably wide composition range, (from 0 to 17 wt. % Bi) and forms fairly smooth and continuous films on room-temperature substrates. The $Pb_{0.71}Bi_{0.29}$ (hcp phase) alloy[9] which is often used by others requires more accurate composition control ($\pm 2\%$) to remain single phase. This latter alloy also forms lumpy or discontinuous films on room-temperature substrates. After evaporation, the photoresist stencil is lifted off in acetone. A perspective drawing of a completed junction is shown in Fig. 4.

It should be noted that the technique described avoids photoresist processing between tunnel barrier formation and subsequent counterelectrode deposition. This eliminates a potential source of contamination. The reduced number of processing steps is also helpful in minimizing the time required to explore different techniques for barrier formation. The process developed also offers the possibility in future experiments of complete junction fabrication without breaking vacuum.

The step-defined process we have developed is analogous in some ways to the process developed by Dolan.[17] The Dolan process employs a suspended photoresist bridge and two depositions from different angles to define the tunnel junction area. However, a careful examination of the Dolan process reveals that it is not well suited to deposition from broad (nonpointlike) sources such as we have with ion-beam deposition. The Dolan process allows nonpoint sources to produce a broad slope of the edge of the deposited film in an area that is critical for junction formation. The thin metal regions associated with this broad slope can contribute to poor tunneling characteristics due to a locally de-

TABLE II. Summary of properties of Ta and Nb based junction properties produced with various oxidation techniques and barrier materials. The measurement temperature is 1.3 K. I_{sg} is the subgap current that flows at 80% of the sum gap voltage; ΔV is the width of the current rise at the sum gap voltage (10% to 90%); R_N is the normal state resistance of the junction; I_c is Josephson critical current; t_{ox} is the oxidation time. The PbBi alloy for all of these junctions is 10 wt. % Bi and 90 wt. % Pb. The symbol ··· means not measured.

Junction	Base electrode	Barrier	Oxidation technique	t_{ox} (min)	R_N (Ω)	ΔV (μV)	$I_{sg}/\Delta I$	I_c (μA)
A	Ta	Ta_2O_5	Glow dsch	0.25	4.3	50	10%	295
		Junction A after annealing[a]			7.4[f]	50	5%	165
B	Ta	Ta_2O_5	Glow dsch	0.33	21	20	1.5%	56
		Junction B after annealing[b]			44[f]	20	1.0%	···
C	Ta	Ta_2O_5	Glow dsch	0.50	317	50	0.5%	1.2
D	Ta	Ta_2O_5	Ion beam	5.0	154	200[c]	10%	2.5
E	Ta	Al_2O_3[d]	133-Pa O_2	20	800	100	3%	···
Nb-A	Nb	Nb-oxide	Glow dsch	0.33	16	200	3%	102
Nb-B	Nb	Nb-oxide	Glow dsch	0.33	19	20	2.5%	82
Nb-C	Nb[e]	Ta_2O_5	Glow dsch	0.33	22	100	5%	55

[a] Annealed in air for 24 min at 80 °C on a hot plate.
[b] Measured at UC Berkeley after several exposures to air (see Fig. 7).
[c] The pure Pb counterelectrode used this junction gives the increased $\Delta V \sim 200\,\mu$V.
[d] Ta base electrode with 50-Å aluminum overlayer.
[e] Niobium base electrode with 70-Å Ta overlayer.
[f] The sensitivity of junction characteristics to air exposure has been eliminated in more recent studies; see text and Ref. 28.

pressed energy gap value. This is not a problem in the step-defined process because the film is abruptly terminated at the step edge and all of the base electrode material near the tunnel barrier is relatively thick (>100 nm). In addition, the step process has a more open geometry which allows easier surface cleaning and oxidation.

III. dc *I-V* CURVES: RESULTS

All of the electrical measurements were made with the junction immersed directly in the LHe bath. The electrical leads were protected with high-frequency filters and shorting switches. The current source employed was capable of ramping the current from negative to positive values smoothly through zero.[18] The ability to ramp through zero was important for our measurements and is not found in most current sources.

A large number of tunnel junctions were fabricated and tested during the development of the step edge process discussed above. Many of the results were far from ideal. Table II provides a representative list of the junctions measured. In Table II, ΔI is taken from the definition $\Delta I = (0.7)V_G/R_N$ where R_N is the normal state resistance of the junction. V_G is defined to be the voltage corresponding to the inflection point of the current rise. V_G is given by the relation $V_G = (\Delta_1 + \Delta_2)/e$ for ideal junctions[15] where Δ_1 and Δ_2 are the energy gaps of the two superconductors. The voltage width ΔV is defined to be the change in voltage required to increase the current at the sum gap from 10% to 90% of ΔI (see Fig. 1). The subgap current I_{sg} is measured at 80% of V_G. The ratio of I_{sg} to ΔI, $I_{sg}/\Delta I$, characterizes the subgap conductance of the junction. The commonly used junction quality parameter V_m[9] is related to $I_{sg}/\Delta I$ by the simple formula $V_m \simeq V_G(2I_{sg}/\Delta I)^{-1}$.

The experiments described in this section present the results of a number of different approaches to junction fabrication. The best solution, dc glow-discharge oxidation, was found after other approaches were tried. Later, we discuss these other techniques, as these may ultimately be useful for other tunnel junctions with different materials. *All of the I-V curves reported were measured in the LHe bath at 1.3 K.* The Josephson current is not indicated on most of the plots so as not to complicate the figures, although it was always present as indicated in Table II. The I_cR_N product for low-resistance Ta junctions is 1.27 mV. For low-resistance Nb junctions $I_cR_N \sim 1.6$ mV. The reduction of the I_cR_N product observed with increasing R_N is consistent with the results of Danchi *et al.*[19]

A. Ta junctions

1. dc glow-discharge oxidation

The properties of Ta junctions produced with glow-discharge oxidation, junctions A, B, and C, are summarized in Table II. All of the junctions that were made with a 20-s oxidation time had resistances within a factor of 2 of each other ($\simeq 20\ \Omega$). This is significant because the data represent the results of three totally different fabrication runs. Other oxidation times also had similarly predictable results. A plot of J_c versus oxidation time is given in Fig. 5.

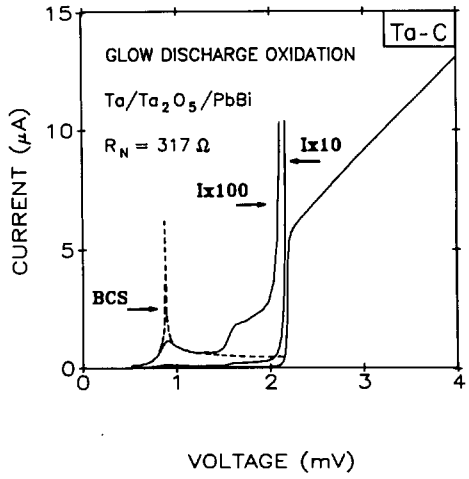

FIG. 6. *I-V* curve of a lower current density ($J_c \sim 200$ A/cm^2) glow-discharge oxidized $Ta/Ta_2O_5/Pb_{0.9}Bi_{0.1}$ junction (junction C in Table II) with the current scales magnified by factors of 10 and 100. The curve labeled BCS is the BCS subgap current ($\times 100$) for two superconductors at 1.3 K [$\Delta_1 = 0.65$ mV (Ta) and $\Delta_2 = 1.5$ mV (PbBi)]. This BCS current is very close to the measured current ($\times 100$) up to Δ_2. See Sec. III A 1 in the text. Junctions with smaller R_N (larger J_c) are required for mixer studies. These lower R_N junctions have larger subgap currents as shown in Fig. 7 and Table II.

I-V curves for two different $Ta/Pb_{0.9}Bi_{0.1}$ junctions produced with the glow discharge process are shown in Figs. 6 and 7 (all measured at 1.3 K). Figure 6 compares the subgap current in one of the best junctions (junction C in Table II) with the predictions of the BCS theory at 1.3 K. Clearly, the current below the $Pb_{0.9}Bi_{0.1}$ gap Δ_2 (~ 1.5 mV) is well fit by the BCS theory (if some noise is present to smooth out the singularity at $\Delta_2 - \Delta_1$). The current rise at Δ_2 may be explained by a combination of multiparticle tunneling and some very small fraction of normal metal inclusions at the Ta interface, as discussed in Sec. IV. The relative importance of these mechanisms is not clearly resolved at this time.

Junctions with higher-current density (lower resis-

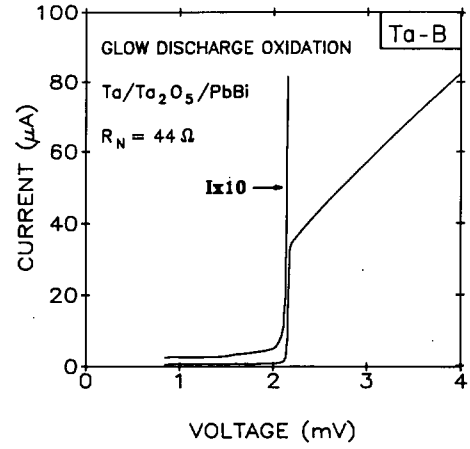

FIG. 7. *I-V* curve for a typical glow-discharge-oxidized $Ta/Ta_2O_5/Pb_{0.9}Bi_{0.1}$ junction as measured at UC Berkeley after several air exposures (junction B). This junction was used for mixer experiments. $J_c = 1500$ A/cm^2. This *I-V* is typical of the other high-quality Ta mixer junctions.

tance) than junction C show an increased subgap current. This effect is seen in Fig. 7 for junction B. The increased sub gap current is always observed. This suggests that there is a universal mechanism that degrades the quality of junctions as the current density is increased beyond $\sim 10^3$ A/cm^2. This trend has been noticed by other workers[7] and is clearly related to the fact that the barrier thickness is approaching a few atomic layers, so that small defects will have a large effect. These problems can be quite subtle and complex and represent an interesting area of study in themselves. Clearly, the modern tools of surface science and well-controlled epitaxial film growth should have a major impact on our understanding of such tunneling systems (see, for example, Ref. 20).

Junction B after air exposure produced strong quantum effects when used as an SIS mixer[3,10,11] (see junction Ta-2 in Ref. 10). Gain $G > 1$ and a noise power within a factor of 2 of the quantum limit at 36 GHz were observed with this junction. The experiments and theoretical modeling in Refs. 10 and 11 show that the low subgap current and "sharp" I-V characteristics of this junction are important for achieving the best mixer performance. (The microwave properties of junction B, before air exposure, were not studied.)

2. Ion-beam oxidized junctions

The small ion source used for cleaning was also used in a large number of attempts to grow an oxide tunnel barrier by ion-beam oxidation. This technique was first used successfully for making SIS tunnel junctions (Nb/PbBi) by Kleinsasser *et al.*[21] and further developed by Pei and van Dover.[22] The basic idea is to take advantage of the directional and well-controlled ion current to grow reproducible and high quality barriers. In this case, low energies (< 200 eV) are desirable for minimizing surface and interface damage in the tunnel barrier.[22] In our system, ion-beam oxidation was performed by adding a small flow of oxygen to the Xe that was flowing into the ion source. Both the Xe and O_2 flows were set with precision leak valves. The O_2 partial pressure was $\sim 2.7\times 10^{-3}$ Pa and the Xe partial pressure was $\sim 2.0\times 10^{-2}$ Pa.

When operating the ion source with O_2/Xe, it was found that tungsten or tantalum filaments lasted for less than 1 h before they burned out. To avoid this problem, several special Thoria-coated iridium filaments were obtained.[23] These filaments are commonly used in ion gauges and have a very long life in oxygen environments. An additional advantage of these filaments is the lower operating temperature required for the same electron emission current.

Despite our best efforts, the Ta junctions produced with ion-beam oxidation were *not very reproducible, nor were they of very high quality*. The I-V characteristic of one of the best ion-beam oxidized junctions (junction D) is shown in Fig. 8(a). The ratio of subgap leakage (I_{sg}) to the current rise at the sum gap (ΔI) in these junctions was almost always $\geqslant 20\%$ for ion-beam oxidized junctions. Junction resistances on the same wafer often differed by a factor of up to 100 and were not reproducible from run to run.

We believe that the irreproducibility of the ion-beam oxidation process is due to the geometry of the step-defined

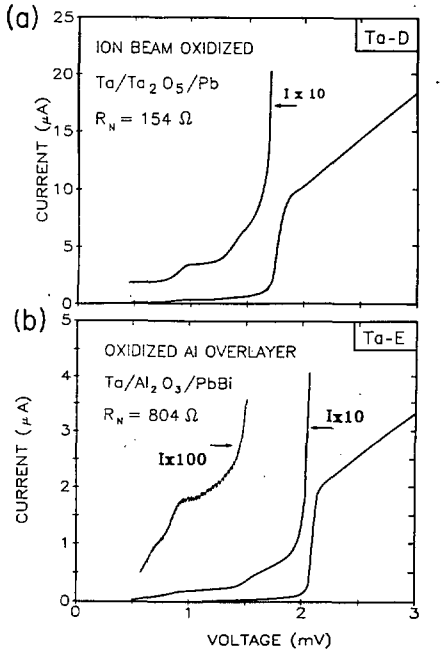

FIG. 8. (a) I-V curve for an ion-beam oxidized Ta/Ta_2O_5/Pb tunnel junction (junction D) showing excess subgap conduction. Note the increased ΔV ($\sim 200\mu$V) with the use of a pure Pb counterelectrode. (b) I-V curve of a Ta/Al/Al_2O_3/$Pb_{0.9}Bi_{0.1}$ overlayer junction (junction E).

technique and the directional nature of the ion beam. Specifically, the large photoresist overhang next to the junction area can shadow the edges of the junction area during the ion-beam cleaning. This shadowing effect leaves portions of the tunnel junction area that are not fully oxidized by the ion beam. This could lead to shorted or low-resistance junctions. Edge effects are important in our process because of the directional nature of ion-beam cleaning and oxidation procedures. With our photoresist geometry, small variations from junction to junction of the ion-beam angle and photoresist edge profile could lead to large variations in junction resistance. A more open geometry, such as the edge[21] or window junction,[9] would be more compatible with ion-beam oxidation.

Despite the disappointing oxidation results, we did learn that the Ta surface can be effectively *cleaned* with the low-energy Xe^+ ion beam. As discussed in the section on Nb junctions, the ability to carefully control the cleaning process (on the Å level) is important in trying to clean a thin (~ 7 nm) Ta overlayer without removing it.

3. Al overlayers on Ta

Al was used as an oxidized metal overlayer barrier on Ta base electrodes to try to improve the tunneling characteristics over those obtained initially with ion beam or thermally oxidized tunnel barriers. Glow-discharge oxidation had not been tried at this point in our research. The Al overlayer technique is now widely used for making high-quality junctions with niobium base and counterelectrodes.[24] One reason that the overlayer technique works so well is that Al wets Nb very well. This technique was not developed when we began our work on Ta junctions. The overlayer technique em-

ployed with our junctions was to follow the standard procedures up to and including the ion-beam surface cleaning prior to oxidation. At this point a thin ($\sim$5 nm) Al film was evaporated onto the Ta surface at $\sim$1 nm/s. After evaporation, pure oxygen was admitted to the chamber to oxidize the Al film surface for $\sim$20 min at a pressure of 133 Pa. No glow discharge was used. After oxidation, the system was reevacuated to a pressure of $\sim 1.3\times10^{-4}$ Pa and a $Pb_{0.9}Bi_{0.1}$ counterelectrode was evaporated at $\sim$4–5 nm/s. Figure 8(b) shows the electrical characteristics of an Al overlayer junction, junction E. The quality of the *I-V* curve is not as high as that achieved with glow discharge oxidation of Ta. Although the Al overlayer technique was not actively pursued in this work, it is a useful starting point for making tunnel junctions with other materials.

B. Niobium tunnel junctions and Ta overlayers on niobium

Several Nb junctions were made with the same glow-discharge oxidation process discussed in Sec. II for Ta junctions. A *typical I-V* curve for one of these Nb junctions is shown in Fig. 9(a) (junction Nb-A). Figure 9(b) (junction Nb-B) shows a very high quality *I-V* curve for a Nb/Nb oxide/$Pb_{0.9}Bi_{0.1}$ junction. This result is not typical, unfortunately.

Ta overlayers on Nb were also prepared, but in a different fashion from the Al overlayers on Ta. A Ta overlayer, $\sim$10 nm thick, was deposited on the Nb film surface in the ion-beam sputter deposition system immediately after deposition of the Nb film. This was accomplished by simply rotating from one sputtering target to the second. Switching targets requires $\sim$1 s. After this, the standard process steps were followed except for a slightly reduced ion cleaning time of 2 rather than 3 min. Figure 9(c) (junction Nb-C) shows the *I-V* characteristic for a Ta overlayer junction. Clearly, the Ta overlayer on niobium improves the sharpness of the current rise at the sum gap compared to the typical result without an overlayer. This improvement is probably due to the suppression of Nb suboxide formation at the interface, as discussed in detail in Refs. 7 and 24 for other overlayers such as Al, Mg, and rare earths. Figure 9(c) also shows that V_G for the Ta overlayer on Nb is lower than V_G for pure Nb. The magnitude of this effect is consistent with the proximity effect model for a 7-nm Ta overlayer on niobium.[25] The slight "knee" above V_G in Fig. 9(c) is also predicted by the proximity effect model.

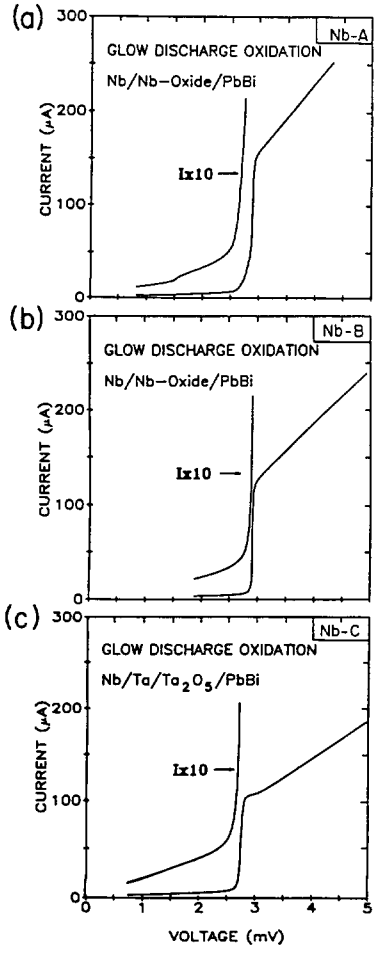

FIG. 9. (a) *I-V* curve of a typical Nb/Nb-Oxide/$Pb_{0.9}Bi_{0.1}$ glow discharge oxidized tunnel junction showing rounding at the gap and subgap leakage current (junction Nb-A). (b) *I-V* curve of an exceptionally good Nb/Nb-Oxide/$Pb_{0.9}Bi_{0.1}$ glow-discharge-oxidized tunnel junction (junction Nb-B). (c) *I-V* curve of Nb based junction with a 7-nm Ta overlayer on the Nb base electrode. The overlayer was oxidized with glow-discharge oxidation and has a $Pb_{0.9}Bi_{0.1}$ counterelectrode (junction Nb-C). Note the reduced value of V_G and the "knee" above V_G due to the proximity effect.

IV. DISCUSSION OF RESULTS

A. Thermal cycling and aging effects

All of the Ta and Nb base electrode junctions survived repeated thermal cycling from room temperature to 4.2 K. If the junction was kept in vacuum or in dry nitrogen during the time at room temperature, the resistance increases were always less than 1%. However, exposure to air caused a gradual increase in the junction resistance which is presumably due to additional oxidation of the junction. An 80°C anneal in air caused the junction resistance to increase by a factor of $\sim$2, as shown for junction A in Table II. This effect is consistent with the work at IBM[26] where the resistance increase was attributed to lateral diffusion of oxygen or water vapor from the junction edges. This problem was solved at IBM by using a PbAuIn alloy counterelectrode.[26] The In is believed to act as a passivating layer, forming an In_2O_3 layer on the surface of the counterelectrode and preventing oxygen diffusion. The PbAuIn alloy was not used in our work because the inclusion of the low T_c phase $AuPb_3$ at the junction interface could broaden the width of the current rise at the sum gap and increase the sub gap current.[27] Recent experiments in our laboratory[28] show that the increasing junction resistance of our Ta/Ta_2O_5/$Pb_{0.9}Bi_{0.1}$ tunnel junctions due to air exposure can be virtually eliminated by evaporating a thin In layer, $\sim$20 nm thick, on top of the $Pb_{0.9}Bi_{0.1}$ counterelectrode immediately after the $Pb_{0.9}Bi_{0.1}$ deposition.

B. Gap suppression at high-current density

Most of the junctions with current densities greater than $\sim 5\times10^3$ A/cm^2 ($R_N < 10\ \Omega$) displayed a negative slope (dI/dV) at the sum gap due to gap suppression. As the current increased, the sum-gap voltage $(\Delta_1+\Delta_2)/e \sim V_G$ decreased. This effect was observed when the junctions were directly immersed in the superfluid helium bath at 1.3 K. For the SIS mixer junctions, $R_N \sim 50$–$100\ \Omega$, we find no gap suppression effects. Gap suppression effects have also been observed by a number of other authors[21,29] using high-current density junctions. In light of the uncertainty in quasi-

particle lifetimes, phonon conduction at interfaces, and similar transport parameters for our system, we are not able to uniquely identify a single mechanism that produces the observed gap suppression effects.

The gap suppression effects that we observe limit the application of our step-defined junctions to current densities of less than $\sim 5\times 10^3$ A/cm^2. Other geometries, such as the window geometry[9,28] and the edge junction geometry[21] offer more effective removal of injected quasiparticles and heat from the junction area. These other geometries allow higher-current densities of up to 10^5 A/cm^2 before nonequilibrium effects are seen.[21] These considerations are important for mixers operating at frequencies above 100 GHz, where J_c should be $> 5\times 10^3$ A/cm^2.

C. Mechanisms for "nonideal" *I-V* curves

A number of physical characteristics of real tunnel junctions can lead to *I-V* curves that deviate from an ideal BCS *I-V* curve. Real tunnel barriers typically vary in thickness, have defects and electron traps, and do not form a sharp metal/insulator interface. Most metal films can also have grain-boundary impurities which may locally reduce the energy gap through the proximity effect. These effects are enhanced in superconductors with short coherence lengths such as Nb and Ta ($\xi \simeq 20$ nm). A brief description of some important mechanisms and their relevance for our junctions is given below.

1. Multiparticle tunneling

Multiparticle tunneling (MPT) is a process in which m particles (two or more) can tunnel at the same time through the barrier.[30] This process is simply a higher-order tunneling process of expected rate $|T|^{2m}$, where T is the tunneling matrix element. The MPT theory predicts a current rise at the m-particle threshold $eV = 2\Delta/m$ of

$$\Delta J_m = \frac{e\Delta}{4\pi\hbar d^2}\tanh\left(\frac{\Delta}{2kT}\right)\left(\frac{e^{-s}}{16}\right)^m \times (s+m^{-1})\left[\left(\frac{2}{m!}\right)\left(\frac{m}{2}\right)^m\right]^2, \quad (1)$$

where $s = 2\kappa d = 1.025\, d\phi^{1/2}$, with d the oxide thickness in Å and ϕ the barrier height in eV. This relation predicts that the current jumps at $2\Delta/m$ will fall off rapidly with increasing m, proportional to $\simeq \exp(-ms)$. From barrier studies with large area Ta tunnel junctions in our laboratory, we know that $d \simeq 15$ Å and $\phi \simeq 1$ eV.[11] This implies that $s \simeq 15$. If this value of s is used to calculate the ratio of the current rise at the $m = 2$ multiparticle tunneling steps ($V = \Delta_1/e$ or Δ_2/e) to the current rise at the sumgap ($m = 1$) we find $\Delta I(m = 2)/\Delta I(m = 1) \simeq \exp(-s) \simeq 3\times 10^{-7}$. As discussed above and as shown in Fig. 6, we typically find a current rise at Δ_1 or Δ_2 which is 10^{-2}–10^{-3} times the current rise at the sum gap. This experimental value for the current ratio is over a factor of 1000 times greater than that predicted by the MPT theory.

The discrepancy between the MPT theory and the experiment may be due to tunneling through locally thin areas of the barrier. If, for example, 15% of the single particle current comes from an area of the junction with a barrier thickness of 5 Å, then we find $\Delta I(m = 2)/\Delta I(m = 1) \simeq 10^{-3}$. This is closer to the experiment. Similar comparisons have been made for subgap currents in small Nb junctions.[31] However, it should be noted that the applicability of the above perturbation theory becomes questionable for such very thin (< 10 Å) barrier regions, where the coupling of the electrodes is strong. Progress has recently been made on the problem of strong electrode coupling,[15,32] although the direct connection with MPT is not clearly resolved.

The MPT theory also predicts the ratio of the $m = 2$ current jumps at Δ_1 and Δ_2. MPT predicts that $I(\Delta_1)/I(\Delta_2) \simeq \Delta_1/\Delta_2 = 0.4$ for $Ta/Pb_{0.9}Bi_{0.1}$, while the data in Fig. 6 for junction C gives a ratio of $\leqslant 0.1$. This value is significantly smaller than the theoretical prediction, as are the ratios for the other *I-V* curves. This discrepancy may also be related to the strong electrode coupling through the barrier, as mentioned above, or to the presence of the additional mechanisms discussed below.

2. Suboxides and normal metal inclusions

The presence of defects and their electrical properties are especially important for the disordered oxide tunnel barriers and interfaces being discussed in this paper. Nb provides a classic example of the problems associated with oxidizing a metal that forms multiple stable oxides. Nb_2O_5 forms most of the barrier thickness. However, suboxides such as NbO and NbO_2 (Ref. 33) form at the metal/oxide interface. NbO is actually a low T_c (~ 1 K) superconductor which may locally depress the gap and give rise to currents that flow at voltages below the gap of bulk clean Nb. Oxygen in solid solution is also well known to strongly depress the T_c of bulk Nb (~ 1 K/at. %)[34] so that oxygen diffusion into Nb at the interface or grain boundaries may also cause local depression of the energy gap.

Studies with thin surface layers of NbO_xC_y (Ref. 35) or Mg (Ref. 36) on Nb show that these layers can act as barriers against the diffusion of oxygen to the Nb surface. Therefore, suboxide formation is reduced. Junction quality is greatly improved with the use of these protective layers.

As originally discussed by Shen,[37] Ta is very different from Nb in that it forms a high quality barrier with simple air oxidation. The lack of stable Ta suboxides[33] suggests that Ta may have a very sharp oxide to metal interface. Studies of the surface oxidation of Ta (Ref. 38) show that Ta is only oxidized in the 3 + (Ta_2O_3) or 5 + (Ta_2O_5) valence state with no evidence for TaO (2 + valence). The exact amount of Ta_2O_3 and its electrical properties may also depend on the oxidation technique so that these results should only be used as a guide. These surface studies[38] are in sharp contrast to similar work on the Nb/Nb-oxide system,[39] where many valence states of Nb are seen. Sputter profiles of anodized Ta and Nb films also reveal a much sharper interface for Ta/Ta_2O_5 than for Nb/Nb_2O_5.[40] This indicates a reduced tendency for oxygen to diffuse into the Ta surface and locally depress the energy gap. The lack of a proximity effect "knee" structure in *all* of the very high-quality Ta junctions in this paper also supports the model of a sharp Ta/Ta_2O_5 interface.

3. Resonant tunneling and barrier defects

Most tunnel barriers have an inherent number of defects due to vacancies and impurities. These defects can produce states in the band gap of the insulator (tunnel barrier) and introduce additional conduction mechanisms besides direct tunneling. Resonant tunneling due to barrier defects has been extensively discussed by Halbritter.[41] Hopping conduction may also be possible for certain defect energy levels. The inelastic nature of the hopping process (loss of energy information) may also allow current to flow for voltages less than the sum gap.

To our knowledge, neither the resonant tunneling mechanism nor the hopping conduction mechanism have been directly correlated with subgap leakage current at this time. However, a recent study of low-frequency noise in Nb/Nb oxide/PbBi tunnel junctions[42] does demonstrate a tentative correlation between the number of "active" defects in the barrier and the *I-V* quality of the junction. The low-frequency noise properties of our high-quality $Ta/Ta_2O_5/Pb_{0.9}Bi_{0.1}$ junctions are currently being investigated and are reported elsewhere.[28] We note that a low density of electron traps is found for many Ta_2O_5 thin films by optical means.[43] This may be related to the high quality junctions that we have been able to produce with Ta base electrodes, although the direct connection is not clear at this time.

4. Gap anisotropy

Energy gap anisotropy is intrinsic to many superconductors and can contribute to a width of the current rise ΔV at the sum gap. Studies of Pb single crystals have shown an energy gap of $\Delta = 1.49$ mV in the 100 direction and $\Delta = 1.25$ mV in the 110 direction.[44] In polycrystalline films, such as those discussed in this paper, variations in the crystal strain as well as microcrystallite orientation can cause a distribution of energy gaps. *We believe that this distribution of Δ's is the cause of the broad (200 μV) current rise always found with pure Pb counterelectrodes.* [See junction D in Table II and Fig. 8(a).]

Impurity scattering can reduce the size of these effects by causing electron scattering to different portions of the Fermi surface, thus averaging the anisotropy.[45] These Fermi surface averaging effects are important in dirty superconductors where the mean free path l is less than the Pippard coherence length ξ_0. For PbBi, $\xi_0 \simeq 100$ nm and $l < 10$ nm. Dirty superconductors such as the PbBi alloy that we use show only one well-defined value of Δ in all of the tunneling experiments to date.[46] This was a major consideration in our choice of $Pb_{0.9}Bi_{0.1}$ as a counterelectrode material. The mean free path in our Nb and Ta films is also quite short ($\simeq 10$ nm $\simeq$ grain size) which should average any anisotropy effects[47] in these materials as well.

5. Quasiparticle lifetime effects

The lifetime of quasiparticles near the superconducting energy gap Δ for temperatures well below T_c is determined by the time it takes to recombine with another quasiparticle of equal and opposite momentum. The recombining quasiparticles form a Cooper pair and emit a phonon of energy $\sim 2\Delta$ in the process. The quasiparticle recombination lifetime is strongly temperature dependent and is given by

$$\frac{1}{\tau_r} \simeq (\pi)^{1/2}\left(\frac{2\Delta(0)}{kT_c}\right)^{5/2}\left(\frac{T}{T_c}\right)^{1/2}\frac{1}{\tau_0}e^{-\Delta/kT}, \qquad (2)$$

where τ_0 is related[48] to the electron-phonon coupling strength λ through the Eliashberg theory. The strong temperature dependence comes from exponential decrease in the number of available quasiparticles as the temperature is decreased. Values of τ_0 have been calculated for various materials[48]: $\tau_0 = 0.2\times10^{-9}$ s for Pb; 1.8×10^{-9} s for Ta; 0.15×10^{-9} s for Nb; and 0.04×10^{-9} s for $Pb_{0.9}Bi_{0.1}$.

As first demonstrated with $Pb_{0.9}Bi_{0.1}$ tunnel junctions,[46] the quasiparticle lifetime can have a significant effect on the width ΔV of the current rise at the sum gap. The temperature-dependent gap width of $Pb_{0.9}Bi_{0.1}$ is well fit[46] by assuming that the temperature-dependent lifetime broadening is given by $\Delta E = \hbar/\tau_r$, where τ_r is given by Eq. (2) with a τ_0 value given above.

For the application of quasiparticle mixers, at low temperatures ($T < 0.3T_c$), quasiparticle lifetime broadening becomes small, and is not a problem for most materials which have a τ_0 much larger than that of $Pb_{0.9}Bi_{0.1}$. However, the mixer experiment at 4.2 K with a Nb/Nb oxide/$Pb_{0.9}Bi_{0.1}$ junction[3,10,11] does have a significant width at the sum gap due to the quasiparticle lifetime of the $Pb_{0.9}Bi_{0.1}$ counterelectrode. The gap width ΔV predicted by the analysis in Ref. 46 is $\Delta V \simeq 150\ \mu$V. Experimentally, we find $\Delta V \simeq 200\ \mu$V. This width has a strong effect on the conversion efficiency of the mixer.[10,11] A PbBi alloy with only 1% or 2% Bi might be preferable for mixers operating at 4.2 K.

V. CONCLUSIONS

We have developed a new step-defined fabrication process for producing small area Ta and Nb based tunnel junctions. The highest-quality $Ta/Ta_2O_5/Pb_{0.9}Bi_{0.1}$ tunnel junctions were produced with a dc glow-discharge oxidation process. These junctions have nearly ideal *I-V* curves and are suitable for observing strong quantum effects in SIS mixer applications. Nb junctions fabricated with the same process have very good, though less ideal, characteristics. The Nb junction characteristics can be improved with the use of a thin Ta overlayer. Several less successful oxidation techniques were also explored and characterized. The effects of a number of physical mechanisms that contribute to the nonideal characteristics of our junctions have been identified. These effects have been compared with the experimental results for Ta and Nb junctions. The relative importance of these different mechanisms is not fully resolved at this time.

ACKNOWLEDGMENTS

We thank J. M. E. Harper and J. J. Cuomo of IBM Research for the use of the small ion source. We appreciate many helpful discussions with J. M. E. Harper, R. B. van Dover, S. I. Raider, R. E. Howard, and A. W. Kleinsasser regarding tunnel junction fabrication and ion-beam processing. We also thank S. I. Raider for suggesting the use of an In overlayer on PbBi in order to reduce aging effects in our

junctions. We also appreciate the initial suggestion from J. M. Rowell and P. L. Richards that we investigate Ta junctions. Many useful discussions with colleagues at Yale, S. T. Ruggiero, and E. K. Track are gratefully acknowledged. This research was supported by NSF Grant Nos. ECS-8305000 and ECS-8604350 and ONR Contract No. N00014-80-C-0855. Fabrication was carried out in the Yale Center for Microelectronic Materials and Structures.

[1]J. R. Tucker and M. J. Feldman, Rev. Mod. Phys. **57**, 1055 (1985).
[2]W. R. McGrath, P. L. Richards, A. D. Smith, H. VanKempen, R. A. Batchelor, D. E. Prober, and P. Santhanam, Appl. Phys. Lett. **39**, 655 (1981).
[3]D. W. Face, D. E. Prober, W. R. McGrath, and P. L. Richards, Appl. Phys. Lett. **48**, 1098 (1986).
[4]L. R. D'Addario, Int. J. Infrared Millimeter Waves **5**, 1419 (1984).
[5]D. P. Woody, R. E. Miller, and M. J. Wengler, IEEE Trans. Microwave Theory Tech. **MTT-33**, 90 (1985).
[6]E. C. Sutton, IEEE Trans. Microwave Theory Tech. **MTT-31**, 589 (1983).
[7]S. I. Raider, IEEE Trans. Magn. **MAG-21**, 110 (1985).
[8]K. H. Gundlach, S. Takada, M. Zahn, and H. J. Hartfusse, Appl. Phys. Lett. **41**, 294 (1982).
[9]Huang, H-C.W., S. Basavaiah, C. J. Kircher, E. P. Harris, M. Murakami, S.P. Klepner, and J. H. Griener, IEEE Trans. Electron Devices **ED-27**, 1979 (1980); see also IBM J. Res. Dev. **24**, pp. 105 (1980).
[10]W. R. McGrath, P. L. Richards, D. W. Face, D. E. Prober, and F. L. Lloyd (unpublished).
[11]D. W. Face, PhD. thesis, Yale University, 1987 (available from University Microfilms).
[12]M. D. Feuer and D. E. Prober, IEEE Trans. Electron Devices **ED-28**, 1375 (1981).
[13]D. W. Face, S. T. Ruggiero, and D. E. Prober, J. Vac. Sci. Technol. A **1**, 326 (1983); see also D. W. Face and D. E. Prober, J. Vac. Sci. Technol. A (to be published).
[14]H. Bispinick, Appl. Phys. **18**, 113 (1979); D. Rosenberg and G. K. Wehner, J. Appl. Phys. **33**, 1842 (1962); N. Laegreid and G. K. Wehner, J. Appl. Phys. **32**, 365 (1961).
[15]G. B. Arnold, J. Low Temp. Phys. **59**, 143 (1985); E. L. Wolf, *Principles of Electron Tunneling Sectroscopy* (Oxford, New York, 1985).
[16]B. Chapman, *Glow Discharge Processes* (Wiley, New York, 1980).
[17]G. J. Dolan, Appl. Phys. Lett. **31**, 337 (1977); see also, L. N. Dunkelberger, J. Vac. Sci. Technol. **15**, 88 (1978).
[18]S. T. Ruggiero, S. Schwarzbek, R. E. Howard, and E. Track, Rev. Sci. Instrum. **57**, 1444 (1986).
[19]W. C. Danchi, J. Bindslev Hansen, M. Octavio, F. Habbal, and M. Tinkham, Phys. Rev. B **30**, 2503 (1984).
[20]A. I. Braginski, J. R. Gavaler, M. A. Janocko, and J. Talvacchio, *Proceedings of the SQUID '85 Conference*, edited by H. D. Hahlbohm and H. Lubbig (de Gruyter, Berlin, 1985), p. 591.
[21]A. W. Kleinsasser, B. D. Hunt, A. C. Callegari, C. Rogers, R. Tiberio, and R. A. Buhrman, IEEE Trans. Magn. **MAG-17**, 307 (1981); A. W. Kleinsasser and R. A. Buhrman, Appl. Phys. Lett. **37**, 841 (1980).
[22]S. S. Pei and R. B. van Dover, Appl. Phys. Lett. **44**, 703 (1984).
[23]Electron Technologies Inc., Kearny, NJ.
[24]H. A. Huggins and M. Gurvitch, J. Appl. Phys. **57**, 2103 (1985); S. Morohashi, H. Shinya, and T. Yamaoka, Appl. Phys. Lett. **48**, 1179 (1985).
[25]S. T. Ruggiero, E. K. Track, D. E. Prober, G. B. Arnold, and M. J. DeWeert, Phys. Rev. B **34**, 217 (1986).
[26]R. F. Broom, S. I. Raider, A. Oosenbrug, R. E. Drake, and W. Walter, IEEE Trans. Electron Devices **ED-27**, 1998 (1980).
[27]S. K. Lahiri, S. Basavaiah, and C. J. Kircher, Appl. Phys. Lett. **36**, 334 (1980).
[28]E. K. Track, A. Worsham, G.-J. Cui, and D. E. Prober, presented at the International Cryogenic Materials Conference, June 1987 [Adv. Cryog. Eng. (to be published)].
[29]J. T. C. Yeh and D. N. Langenberg, Phys Rev. B **17**, 4303 (1978); D. Winkler and T. Claeson, Phys. Scr. **32**, 317 (1985).
[30]L. E. Hasselberg, M. T. Levinsen, and M. R. Samuelsen, Phys. Rev. B **9**, 3753 (1974); P. Mukhopadhyay, J. Phys. F **9**, 903 (1979).
[31]W. J. Gallagher, S. I. Raider, and R. E. Drake, IEEE Trans. Magn. **MAG-19**, 807 (1983); P. W. Epperlein, Physica **108B**, 999 (1981).
[32]T. M. Klapwijk, G. E. Blonder, and M. Tinkham, Physica **109+110B**, 1157 (1982).
[33]G. V. Samsonov, Ed., *The Oxide Handbook* (Plenum, New York, 1982).
[34]C. C. Koch, J. O. Scarbrough, and D. M. Kroeger, Phys. Rev. B **9**, 888 (1974).
[35]T. S. Kuan, S. I. Raider, and R. E. Drake, J. Appl. Phys. **53**, 7464 (1982).
[36]J. Kwo, G. K. Wertheim, M. Gurvitch, D. N. E. Buchanan, IEEE Trans. Magn. **MAG-19**, 795 (1983).
[37]L. Y. L. Shen, in *Superconductivity in d- and f-Band Metals*, edited by D. H. Douglass (Plenum, New York, 1972).
[38]F. J. Himpsel, J. F. Morar, F. R. McFeely, R. A. Pollak, and G. Hollinger, Phys. Rev. B **30**, 7236 (1984).
[39]R. A. Pollak, H. J. Stolz, S. I. Raider, and R. F. Marks, Oxid. Met. **20**, 185 (1983).
[40]K. Sasaki and T. Umezawa, Thin Solid Films **74**, 83 (1980).
[41]J. Halbritter, IEEE Trans. Magn. **MAG-21**, 858 (1985).
[42]C. T. Rogers and R. A. Buhrman, IEEE Trans. Magn. **MAG-21**, 126 (1985); C. T. Rogers, Ph.D thesis, Cornell University, 1987.
[43]J. H. Thomas III, J. Appl. Phys. **45**, 5349 (1974); S. Seki, T. Unagami, and B. Tsujiyama, J. Vac. Sci. Technol. A **1**, 1825 (1983).
[44]G. I. Rochlin, Phys. Rev. **153**, 513 (1967).
[45]D. Markowitz and L. P. Kadanoff, Phys. Rev. **131**, 563 (1963); C. K. Campbell, R. C. Dynes, and D. G. Walmsley, Can. J. Phys. **44**, 2601 (1966).
[46]R. C. Dynes, V. Narayanamurti, and J. P. Garno, Phys. Rev. Lett. **41**, 1509 (1978).
[47]S. M. Durbin, D. S. Buchanan, and J. E. Cunningham, and D. M. Ginsberg, Phys. Rev. B **28**, 6277 (1983).
[48]S. B. Kaplan, C. C. Chi, D. N. Langenberg, J. J. Chang, S. Jafarey, and D. J. Scalapino, Phys. Rev. B **14**, 4854 (1976).